



**Computational Insights into the Interaction of Water with
the UiO-66 Metal-Organic Framework and Its Functionalized
Derivatives**

Journal:	<i>Journal of Materials Chemistry C</i>
Manuscript ID	TC-ART-04-2023-001313.R1
Article Type:	Paper
Date Submitted by the Author:	04-Jul-2023
Complete List of Authors:	Zhang, Jierui; UNSW, Chemistry Paesani, Francesco; University of California San Diego, Lessio, Martina; UNSW, Chemistry

Computational Insights into the Interaction of Water with the UiO-66 Metal-Organic Framework and Its Functionalized Derivatives

Jierui Zhang^a, Francesco Paesani^{b*}, Martina Lessio^{a*}

^a School of Chemistry, The University of New South Wales, Sydney, NSW 2052, Australia

^b Department of Chemistry and Biochemistry, University of California San Diego, La Jolla,
CA, United States.

*Corresponding authors: martina.lessio@unsw.edu.au, fpaesani@ucsd.edu

Abstract

The UiO-66 metal-organic framework (MOF) has been identified as a promising hydrophilic material for water harvesting. Recent studies show that its water uptake ability at low relative humidity (RH) can be improved by incorporating hydrophilic functional groups into the framework. In this work, we provide computational insights into the adsorption of water in UiO-66 and its functionalized derivatives to reveal the role played by different adsorption sites and functional groups in the adsorption mechanism. We started by developing molecular models for UiO-66, UiO-66-NH₂, UiO-66-OH, and UiO-66-(OH)₂ compatible with the MB-pol data-driven many-body potential of water. We then benchmarked these models against *ab initio* data. We used these models to perform molecular dynamics simulations and calculate radial distribution functions, IR spectra, and two-dimensional density distribution maps for

water in the MOFs. These results consistently show that the μ_3 -OH sites are the preferential interaction sites for water in UiO-66 and all its variants, and the formation of localised water clusters inside the octahedral pores is responsible for the abrupt step in the experimental adsorption isotherms. Furthermore, the presence of functional groups in the framework allows water to cluster in the octahedral pores at lower RH, thus making the MOF a more efficient water harvester. Overall, this study provides molecular-level insights into the pore filling process of UiO-66 and its functionalized derivatives, which are needed for the design of efficient water harvesting materials based on MOFs.

Introduction

Freshwater is an essential resource for human lives and is needed for many critical aspects, such as drinking, energy production, irrigation, and industry. Currently, around two-thirds of the world's population suffer severe clean freshwater shortage for at least one month each year.¹ The shortage of freshwater is thus a significant global concern exacerbated by the growing world population, expansion of agriculture irrigation, and increasing industrial pollution. Generally, wastewater purification and seawater desalination plants are located in coastal regions and long-distance transportation is required to deliver freshwater to inland and higher mountain regions.² Thus, the exploitation of new readily accessible water resources is crucial for the expansion of freshwater availability to address the water scarcity issue worldwide. Water is present in the air in the form of vapor and droplets. This atmospheric water represents a potential source of freshwater that is not restricted by geographical conditions and could provide more freshwater than all the rivers on Earth.³ The development of efficient atmospheric water harvesting methods is thus a critical step towards addressing the growing demand for freshwater resources. The methods currently available such as conventional fog

capture and dewing require either large energy inputs or high relative humidity (RH) which make their application in arid regions unfeasible.⁴⁻⁶ Therefore, an ideal atmospheric water harvesting system should be able to collect water from dry air (low RH) with a low energy supply.

Recently, metal-organic frameworks (MOFs) have garnered significant interest in the scientific community as promising water harvesters.⁷ MOFs are crystalline porous materials constructed from inorganic secondary building units (SBUs) and organic linkers. The MOF properties are determined by the linkers and SBUs topologies, with thousands of combinations discovered to date.⁸ This offers a systematic way to design an ideal water harvester with high stability,^{7,9-11} high water capacity,^{7,12-14} low energy consumption,^{7,15-17} and high water affinity with hydrophilic functional groups (*e.g.* -OH) incorporated within the framework.¹⁸⁻²¹ In spite of these promising features, the application of MOFs in water harvesting technologies is still an emerging area of research and more fundamental insights into the adsorption mechanisms are required in order to scale up this technology.

UiO-66 is a well characterized and established hydrophilic water-stable MOF. It is composed of zirconium oxide SBUs ($Zr_6O_4(OH)_4$) that are 12-fold connected in a face-centered-cubic arrangement by 1,4-benzenedicarboxylic acid (H_2BDC) organic linkers.¹⁰ The high connectivity and strong Zr-O coordination bonds within the SBU contribute to the outstanding water stability of UiO-66.^{10,22} Experimental studies have demonstrated that UiO-66 can undergo multiple water adsorption-desorption cycles with steady adsorption performance and minimum distortion of the structure.^{7,11,23} In addition, the water adsorption isotherms of UiO-66 can be tuned by introducing hydrophilic functionalized BDC linkers, which allow for significantly improving the adsorption ability at lower RH.¹⁸⁻²⁰ Overall, the outstanding stability, reversible water uptake ability, and the possibility to tailor the physical

and chemical properties of UiO-66 through functionalization make it an extremely promising material for water harvesting and an excellent system to study in order to develop improved MOFs for water harvesting.

Computational chemistry methods are widely applied and effective tools for the study of MOFs due to their predictive power and their ability to provide molecular-level insights inaccessible to experiments.^{24–26} Previous computational studies of UiO-66 have employed generic force fields^{13,21,27,28} to conduct classical molecular dynamics (MD) simulations aimed at understanding the key water-MOF interactions and the diffusion process of water across the MOF cavities. An exception to this, is the vibrational spectroscopy study of water within defective UiO-66 performed by Caratelli *et al.* using *ab initio* MD simulations.²⁹ In this work, we introduce a family of force fields for UiO-66 and its functionalized derivatives that are derived from *ab initio* data and can model the frameworks as flexible objects. Recent simulation studies investigating the influence of guest molecule adsorption in the UiO-66 framework have highlighted the importance of considering framework flexibility to accurately reproduce experimental results.³⁰ These newly developed force fields are specifically designed to be compatible with the MB-pol data-driven many-body potential for water.^{31–34} MB-pol has been shown to accurately predict the properties of water from the gas to the condensed phases.^{34–37} We employ the newly developed force fields in MD simulations to investigate structural and dynamical properties of water in UiO-66 and its functionalized derivatives. In particular, we compute radial distributional functions (RDF), two-dimensional density distribution maps, and infrared (IR) spectra for water as a function of RH. These computed properties provide general insights into the pore filling process and the driving force that initiates water adsorption and the formation of water clusters within the frameworks. Moreover, the dynamical properties help us unravel the influence of -NH₂, -OH and -(OH)₂ functionalization on the MOF's water adsorption ability. The understanding of these

mechanisms at the molecular level is critical to establishing design principles of new porous materials for atmospheric water harvesting purposes with improved water adsorption abilities.

Computational details

Force field

We developed a family of force fields for UiO-66 and its functionalized derivatives by using a genetic algorithm (GA)³⁸ to fit all the parameters describing the UiO-66 SBU and the framework-water interactions to reference energies obtained from density functional theory (DFT)^{39,40} calculations.³⁸ The DFT reference energies were obtained for a cluster model of the UiO-66 framework representing the local environment around the inorganic metal node. The cluster model was prepared by truncating the periodic MOF structure and replacing the 12 BDC linkers with formate capping groups (Figure S1). This cluster structure includes all the relevant atoms for an accurate description of all the interaction sites for hydrogen-bonding with water. These include the linker carboxylate oxygen atoms (O_{linker}), the hydroxide group ($\mu_3\text{-OH}$) and the oxygen atoms ($\mu_3\text{-O}$) interconnecting the Zr atoms (Figure S1).

The periodic MOF structure was optimized using the Vienna Ab initio Simulation Package (VASP)^{41–44} with the PBE functional and Grimme's D3 dispersion correction.^{45–47} The electronic wavefunction was described using a plane-wave basis with 700 eV kinetic energy cutoff and the projector-augmented-wave (PAW) potentials available in VASP. The Brillouin zone was sampled using a $2 \times 2 \times 2$ k-point mesh generated based on the Monkhorst–Pack scheme. All the calculations involving the metal node cluster were performed with the ω B97X-D3BJ functional^{46–49} using the ORCA software package (version 5.0.1).^{50–52} Geometry optimizations were performed using the def2-SVP^{53,54} basis set for all the atoms except for Zr

atoms. A larger def2-TZVPP^{53,54} basis set and the effective core potential def2-ECP⁵⁵ were used to describe the valence and core electrons for Zr atoms, respectively. Single-point energy refinements were performed using the def2-TZVPP^{53,54} basis set for all atoms and the def2-TZVPP^{53,54} basis set (with the def2-ECP) for the Zr atoms.

The bonded force field parameters for the UiO-66 inorganic units were fitted to single-point energies of 300 configurations of the cluster model with one of the Zr atoms distorted relative to its equilibrium position. The bonded force field parameters for the atoms of the organic linkers were extracted from the General Amber Force Field (GAFF).⁵⁶ In addition, the bond force constants for the N-H and O-H groups of BDC-NH₂, BDC-OH and BDC-(OH)₂ were modified to align with the experimental infrared (IR) spectra for UiO-66-NH₂,⁵⁷⁻⁵⁹ UiO-66-OH and UiO-66-(OH)₂ (Figure S3).⁵⁹⁻⁶¹ In the simulations, only the neutral state of these functional groups has been considered. The occurrence of proton exchange reactions between MOFs and water is influenced by the phase of water and the pH of the environment, and it is important to note that the adsorbed water cannot be definitively categorized as either liquid or gas.⁶² In gas phase, the ionic dissociation energy of water is observed to be prohibitively high.⁶³⁻⁶⁵ On the other hand, studies on -NH₂, -OH and -(OH)₂ functionalized MOFs exposed to liquid water at neutral pH show that the protonation or deprotonation of these groups does not occur.⁶⁶⁻⁶⁸ The many-body potential energy function (MB-pol)³¹⁻³⁴ was used to model water within the system. MB-pol has been shown to accurately reproduce the properties of water for both gas and condensed phases,³⁴⁻³⁶ which is well suited for an accurate representation of the properties of water adsorbed in MOFs.^{62,69,70}

All Lennard-Jones (LJ) force field parameters were taken from GAFF⁵⁶ except for Zr for which the parameters were obtained from the Universal Force Field (UFF).²⁷ The LJ parameters for the description of the interaction between different atom types were derived

using Lorentz-Berthelot mixing rules.⁷¹ When applying Lorentz-Berthelot mixing rules⁷¹ to the interactions involving water, the LJ parameters of the TIP4P/2005 water model⁷² were used since TIP4P/2005 is the closest empirical water model to MB-pol.^{62,69,70} This strategy has proven successful in previous MD simulations incorporating MB-pol water model to study water-MOF interactions.^{62,70,73} In addition, Buckingham force field parameters describing the van der Waals (vdW) interactions between the oxygen atoms (OW) of the water molecules with μ_3 -OH, and the hydrogen atoms (HW) of the water molecules with μ_3 -O and O_{linker} interaction sites were specifically fitted to DFT reference energies using the GA to obtain a more accurate representation of these interactions. To this end, we first optimized cluster model structures with a water molecule hydrogen-bonded to the μ_3 -OH, μ_3 -O and O_{linker} sites (Figure S4). These geometry optimizations were performed with constraints applied to the entire cluster model in order to maintain the rigidity of the framework. We then generated 110 configurations with the water molecule located at varying distances from the μ_3 -OH, μ_3 -O and O_{linker} interaction sites for which the interaction energies were calculated at the DFT level of theory and corrected for the basis set superposition error (BSSE) using the counterpoise method.^{74,75} Finally, the partial charges of the atoms in the metal node and organic linkers were calculated using the Charge Model 5 (CM5)⁷⁶ as implemented in Gaussian 16⁷⁷ with the same DFT functional and basis set used for the single point energy refinements.

Molecular dynamics simulations

All MD simulations were performed with an in-house software based on the DL_POLY_2 simulation package⁷⁸ using the force fields described in the previous sections for all MOF variants and the MB-pol^{31–34} model for water. The equations of motions were propagated using the velocity-Verlet algorithm⁷⁹ with a time step of 0.2 fs³³ and the non-bonded interactions were truncated at 9.0 Å with long-range electrostatics calculated by Ewald

summation,⁸⁰ the time step was established according to the study by Medder *et al.*³³ The initial configurations of UiO-66 and its functionalized derivatives interacting with water molecules were generated using PACKMOL.⁸¹ The number of water molecules in the MOF structure at different RH values was derived from the experimental water adsorption isotherm for UiO-66 (see Section 3 in the Supporting Information).¹¹ The water molecules were randomly distributed into the $1 \times 1 \times 1$ cubic unit cell of the UiO-66 framework (20.7465 Å cell parameter). Each system went through a randomization at 1000 K and 1 atm for 10 ps, followed by a 40 ps gradual cooling process carried out in the isothermal-isobaric ensemble (constant number of atoms, pressure, and temperature, *NPT*) at 1 atm and 500 K for 20 ps, and at 1 atm and 298 K for 20 ps. The production runs were then carried for 1 ns in the *NPT* ensemble at 1 atm and 298 K. In all *NPT* simulations the temperature was controlled using a massive Nosé-Hoover chain thermostat where each degree of freedom was coupled to a Nosé-Hoover thermostat chain of length four, while the pressure was controlled by a Nosé-Hoover barostat based on the algorithm introduced by Tuckerman.⁷⁹ The RDFs, two-dimensional density distribution maps, and infrared spectra were averaged from five independent trajectories of 50 ps carried out in the microcanonical ensemble (constant number of atoms, volume, and energy, *NVE*) with the volume fixed at the average value calculated from previous *NPT* simulations.

Theoretical infrared spectra

The infrared (IR) spectra of water adsorbed in the different UiO-66 variants were calculated according to

$$I = \left[\frac{2\omega}{3V\hbar c\epsilon_0} \right] \tanh\left(\frac{\hbar\omega}{k_B T}\right) \int_{-\infty}^{\infty} e^{i\omega t} \langle \mu(0)\mu(t) \rangle dt \quad (1)$$

where V is the system volume, \hbar is the reduced Planck's constant, c is the speed of light, ϵ_0 is the permittivity of free space, k_B is the Boltzmann's constant, T is the simulation temperature, and $\langle \mu(0)\mu(t) \rangle$ is the (ensemble-averaged) dipole-dipole time correlation function. The dipole moment of water (μ in Eq. 1) was represented by the many-body dipole moment function (MB- μ).^{36,37} The MB- μ depends also on the induced dipole moment created when MOF atoms polarize the MB-pol water molecules.^{36,37} Since all MD simulations were carried out at the classical level, the simulated spectra IR were red-shifted by 60 cm^{-1} and 175 cm^{-1} in the H-O-H bending and O-H stretching regions, respectively, to effectively account for zero-point energy effects as discussed in the studies by Medders *et al.*^{36,37}

Results and discussion

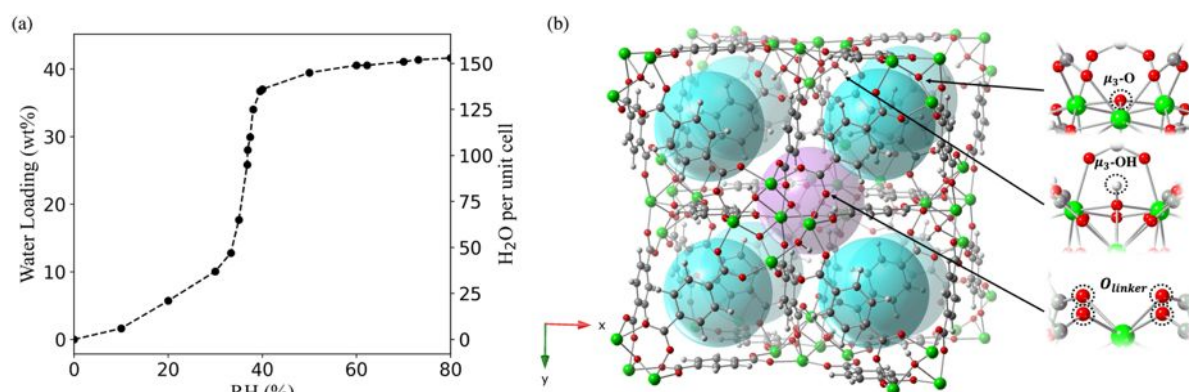


Figure 1: (a) The experimental adsorption isotherm of UiO-66 at 0-80% relative humidity (RH) and room temperature. The left y-axis represents the weight percentage (wt%) of water in the MOF measured experimentally, while the right y-axis represents the number of water molecules per UiO-66 unit cell included in the simulation. Data sourced from Furukawa *et al.*¹¹ (b) Pores and bonding sites for water adsorption in UiO-66; each octahedral pore (purple sphere) is surrounded by eight tetrahedral pores (blue spheres); the three bonding sites ($\mu_3\text{-OH}$, $\mu_3\text{-O}$ and O_{linker}) available for water in the pores are labelled with black arrows.

UiO-66 has a type V isotherm (Figure 1a), displaying a gradual increase in water adsorption at 10-30% RH, followed by a sudden rise at 30% RH. The first step towards a molecular-level understanding of the pore filling process behind these experimental observations is the identification of the possible interaction sites for water. There are two types of cavities within UiO-66, the octahedral and the tetrahedral pores. Each octahedral pore is interconnected to eight tetrahedral pores.^{10,22} The octahedral and tetrahedral pores in UiO-66 provide different interaction environments for water (Figure 1b). In the octahedral cavity, the O_{linker} from the BDC ligands are the only accessible sites for the formation of hydrogen-bonding interactions with water. In contrast, water molecules in the tetrahedral pores can interact with the $\mu_3\text{-O}$ and $\mu_3\text{-OH}$ sites, in addition to the O_{linker} sites.^{10,22}

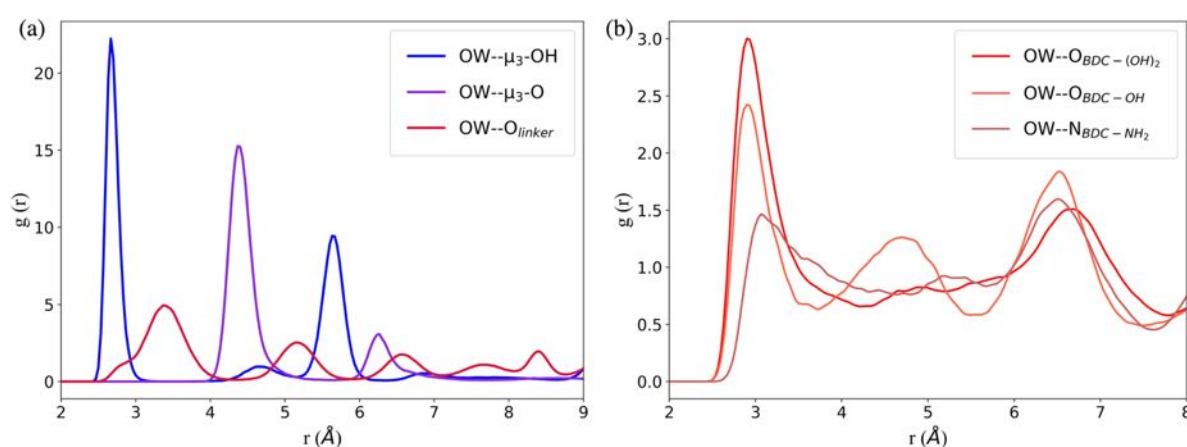


Figure 2: The radial distribution function (RDF) between the oxygen of water (OW) and the oxygen or nitrogen atoms in (a) the $\mu_3\text{-OH}$, $\mu_3\text{-O}$ and O_{linker} interaction sites in UiO-66 and (b) in the $-\text{NH}_2$ and $-\text{OH}$ function groups in the three functionalized derivatives of UiO-66. All plots were obtained from simulations with the same number of water molecules per unit cell as UiO-66 at 10% relative humidity (RH).

The RDFs between the oxygen atom (OW) of water and the oxygen atoms of the interaction sites within UiO-66 at 10% RH were calculated to determine the initial binding sites (Figure 2a). The RDF describing the spatial correlation between the oxygen atoms of the water molecules (OW) and the oxygen atoms of the $\mu_3\text{-OH}$ groups peaks at a shorter distance (2.7 Å)

compared to the corresponding peaks in the RDFs between OW and the oxygen atoms of μ_3 -O (4.4 Å) and O_{linker} (3.4 Å). This reveals that the affinity between water and the three interaction sites on the SBUs follows the trend: $\mu_3\text{-OH} > O_{\text{linker}} > \mu_3\text{-O}$. Furthermore, the amplitude of the $\text{OW}\cdots\mu_3\text{-OH}$ RDF is significantly higher compared to that of the $\text{OW}\cdots O_{\text{linker}}$ RDF, thus confirming that the $\mu_3\text{-OH}$ is the most favorable binding site at low RH. This finding is consistent with previous computational studies showing that water preferentially binds to the $\mu_3\text{-OH}$ in UiO-66.^{13,21,28,29} Moreover, this aligns with the experimental observation that $\mu_3\text{-OH}$ is the primary adsorption site for water in MOF-801, a MOF containing the same inorganic SBUs as UiO-66.¹¹ Although the RDF peak positions show that the O_{linker} is more attractive to water compared to the $\mu_3\text{-O}$, the intensity of $\text{OW}\cdots\mu_3\text{-O}$ RDF is significantly higher compared to $\text{OW}\cdots O_{\text{linker}}$. This apparent contradiction is easily explained by the fact that the $\mu_3\text{-O}$ sites are present in the tetrahedral cavities with the $\mu_3\text{-OH}$ sites; the two peaks at 4.4 Å and 6.5 Å for the $\text{OW}\cdots\mu_3\text{-O}$ correspond to the distance between the $\mu_3\text{-O}$ and the water molecules bonded to neighboring $\mu_3\text{-OH}$ sites. Hence, at 10% RH water does not bind to the $\mu_3\text{-O}$ sites in UiO-66.

In the functionalized UiO-66 MOFs the $-\text{NH}_2$, $-\text{OH}$ and $-(\text{OH})_2$ functional groups are the secondary preferential bonding sites, with the RDFs between OW and the nitrogen or oxygen atoms in the $-\text{NH}_2$ (3.0 Å), $-\text{OH}$ (2.9 Å) and $-(\text{OH})_2$ (2.9 Å) functional groups peaking at a larger distance compared to $\mu_3\text{-OH}$ (2.7 Å) and at a lower distance compared to O_{linker} (3.4 Å), as shown in Figure 2b. We note that the $\text{OW}\cdots\mu_3\text{-OH}$ and $\text{OW}\cdots O_{\text{linker}}$ RDFs for the functionalized MOFs (Figure S7) peak at the same distance as for UiO-66.

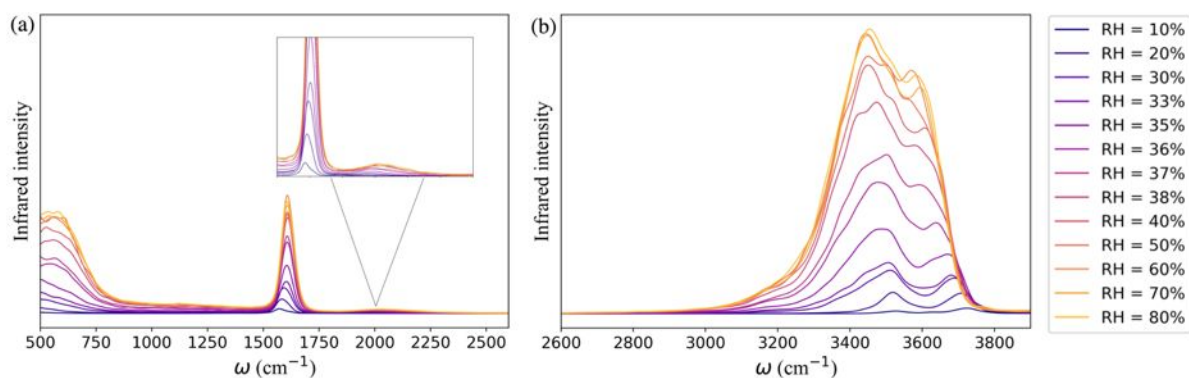


Figure 3: The theoretical IR spectra of water within the UiO-66 confinement at 10-80% RH in the range (a) 500-2600 cm^{-1} and (b) 2600-3900 cm^{-1} .

The simulated IR spectra of water in the framework as a function of RH monitors the change in the hydrogen-bonding topology of water confined in the MOF pores at the different stages of the adsorption process. In Figure 3a, the far infrared region ($< 1000 \text{ cm}^{-1}$) describes the collective librational modes (*i.e.*, rocking, wagging, and twisting motion) of water that are difficult to isolate. The peak around 1650 cm^{-1} represents the H-O-H bending mode of water which aligns with the experimentally observed water bending signal.^{82,83} The relatively weak and wide band centered at 1979 cm^{-1} (highlighted in the inset of Figure 3a) is the combination band that arises from the coupling of the bending vibration with one or more librational modes. Beyond 2600 cm^{-1} the IR spectrum is characterized by the broad band of hydrogen-bonded ($3400\text{-}3500 \text{ cm}^{-1}$) and non-hydrogen-bonded ($\sim 3713 \text{ cm}^{-1}$) O-H stretching vibrations of water adsorbed in the MOF pores (Figure 3b). The latter arises at low RH due to the presence of water molecules bound to the $\mu_3\text{-OH}$ groups of the framework which are not hydrogen-bonded to other water molecules. As RH increases, an extended hydrogen-bonding network forms, which weakens the intramolecular bond of water. This leads to a red-shift of the free O-H stretch and a broadening of the band in the $3400\text{-}3500 \text{ cm}^{-1}$ region.

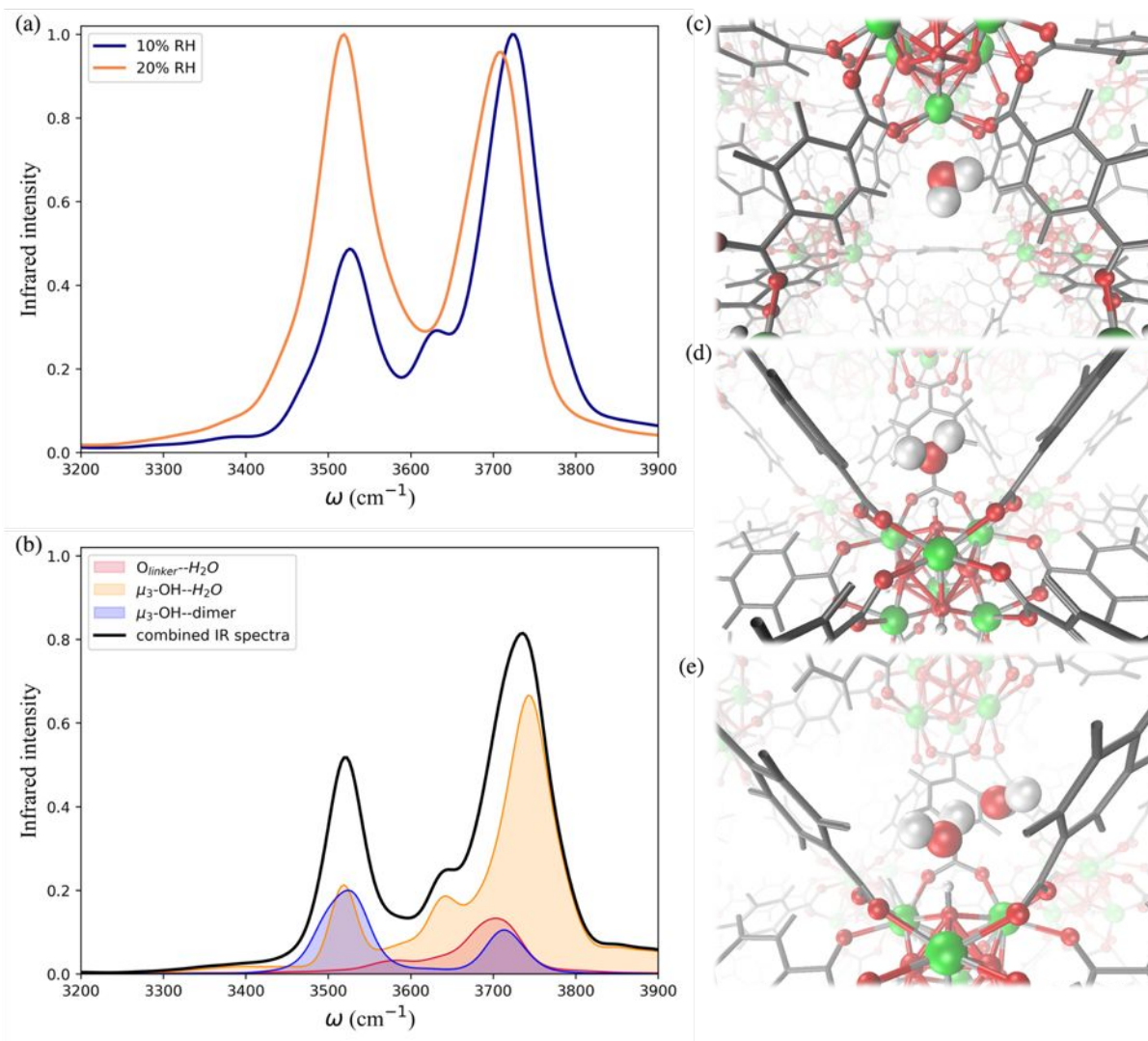


Figure 4: (a) Calculated IR spectra of water within UiO-66 at 10% relative humidity (RH) and 20% RH in the O-H stretching region. (b) Breakdown of the contributions to the IR spectrum at 10% RH from water locating around the μ_3 -OH sites (yellow), water interacting with the O_{linker} group (red), and water dimers interacting with the μ_3 -OH sites (blue); the solid black line represents the combined IR spectrum resulting from summing these contributions. MD simulation snapshots showing water located around the (c) O_{linker} and (d) μ_3 -OH sites, as well as (e) a water dimer located around the μ_3 -OH site. Zr atoms are represented by green spheres, O atoms by red spheres, H atoms by white spheres, and the benzene rings by grey lines.

To further investigate the hydrogen-bonding connectivity in the pores of pristine UiO-66, we calculated the IR spectra of water molecules located at different interaction sites within the MOF pores (Figure 4b) at 10% RH where the contribution of water-MOF and water-water

interactions can be identified more easily. Based on the RDFs, μ_3 -OH and O_{linker} are the preferential binding sites at 10% RH, where approximately 67% and 13% of the water are located around the μ_3 -OH sites and O_{linker} , respectively. When interacting with the O_{linker} , water acts as a hydrogen-bond donor, which gives rise to the non-hydrogen-bonded O-H stretch and the hydrogen-bonded O-H stretch in the IR spectrum (Figure 4a) at $\sim 3713\text{ cm}^{-1}$ and $\sim 3582\text{ cm}^{-1}$, respectively.^{10,59} The water hydrogen-bonded to the μ_3 -OH acts as a hydrogen-bond acceptor, resulting in symmetric ($\sim 3632\text{ cm}^{-1}$) and asymmetric ($\sim 3743\text{ cm}^{-1}$) O-H stretches. Interestingly, because of the electric coupling associated with the hydrogen bond between the μ_3 -OH group and water, the O-H stretching of water also reports on the vibration of μ_3 -OH at 3526 cm^{-1} (Figure 4a), which is in agreement with the vibrational frequency of μ_3 -OH measured experimentally for UiO-66.^{10,59} We determined the IR signal of water induced by the vibration of the hydrogen-bond donating interaction sites on the framework (*e.g.*, μ_3 -OH) by labeling the H atoms of the sites with deuterium (D) (refer to Section 4 in Supporting information). The symmetric and asymmetric O-H stretch signals are only significant at low water loading (*i.e.*, 10% RH) since under these conditions water is not donating hydrogen bonds to neighboring water molecules.⁸⁴ The remaining water molecules (approximately 20%) are part of water dimers interacting with μ_3 -OH sites. These involve a water molecule accepting a hydrogen-bond from a μ_3 -OH site while donating a hydrogen-bond to a neighboring water molecule. The signal at 3526 cm^{-1} is contributed by the hydrogen-bonded O-H stretch of the water dimer, while the non-hydrogen-bonded free O-H stretch can be observed at 3713 cm^{-1} . All these observed vibrational modes of water are consistent with a recent study by Zhang *et al.*,⁸⁴ where they selectively measured the IR signals of the different O-H stretches in a water dimer.⁸⁴

As the water loading increases at 20% RH, there are two main signals with similar intensity around 3500 and 3700 cm^{-1} (Figure 4a). These peaks correspond to the vibrational signals of water dimers just discussed. In addition, the symmetric ($\sim 3632\text{ cm}^{-1}$) and asymmetric

vibrations ($\sim 3743\text{ cm}^{-1}$) corresponding to water acting as a hydrogen-bond acceptor have been weakened. These results indicate that an extended formation of hydrogen-bonds between water molecules occurs at 20% RH. Overall, the IR spectra of water in UiO-66 show that at low water loading (10% RH), the μ_3 -OH is the primary binding site and the formation of water dimers bonded to this site outweighs the interaction of water with the O_{linker} sites. As the water loading increases additional water tends to form water clusters around the μ_3 -OH site.

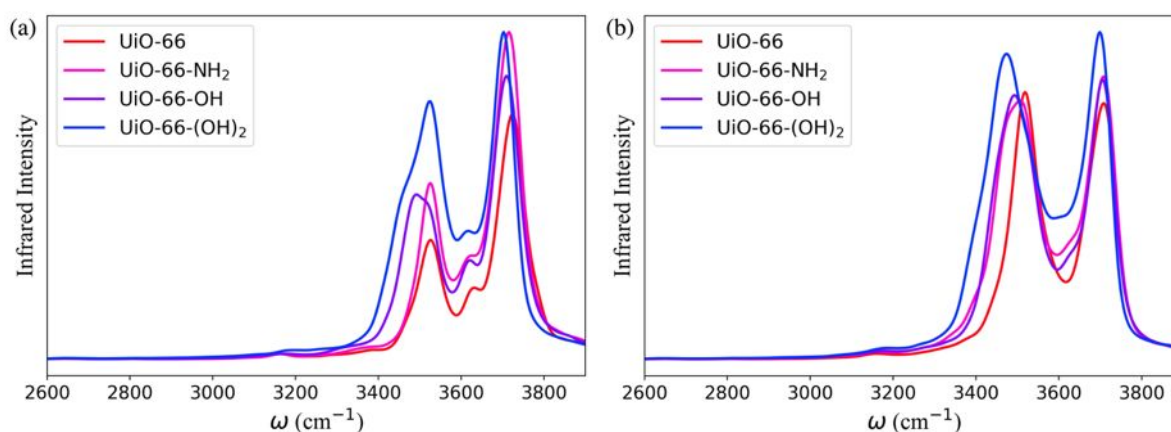


Figure 5: The theoretical IR spectra of water within UiO-66 and its -NH₂, -OH and -(OH)₂ functionalized derivatives, calculated with the same number of water molecules per unit cell as UiO-66 at (a) 10% and (b) 20% relative humidity (RH) in the range 2600-3900 cm^{-1} .

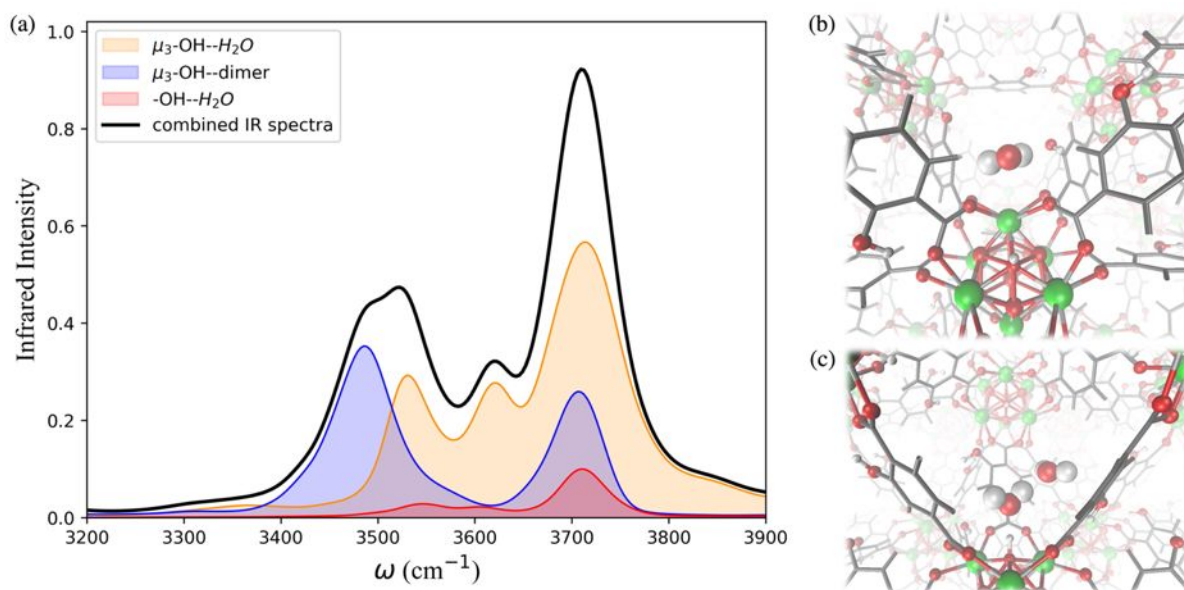


Figure 6: (a) Breakdown of the contributions to the IR spectrum of UiO-66-OH at 10% relative humidity (RH) from single water molecules locating around the μ_3 -OH sites, water interacting with the -OH functional group, water dimers occupying the μ_3 -OH sites, and the combined IR spectra resulting from summing these contributions; MD simulation snapshots showing (b) the water locating around the -OH functional group and O_{linker}; (c) the water dimer locating around the μ_3 -OH interaction sites. Zr atoms are represented by green spheres, O atoms by red spheres, H atoms by white spheres, and the benzene rings by grey lines.

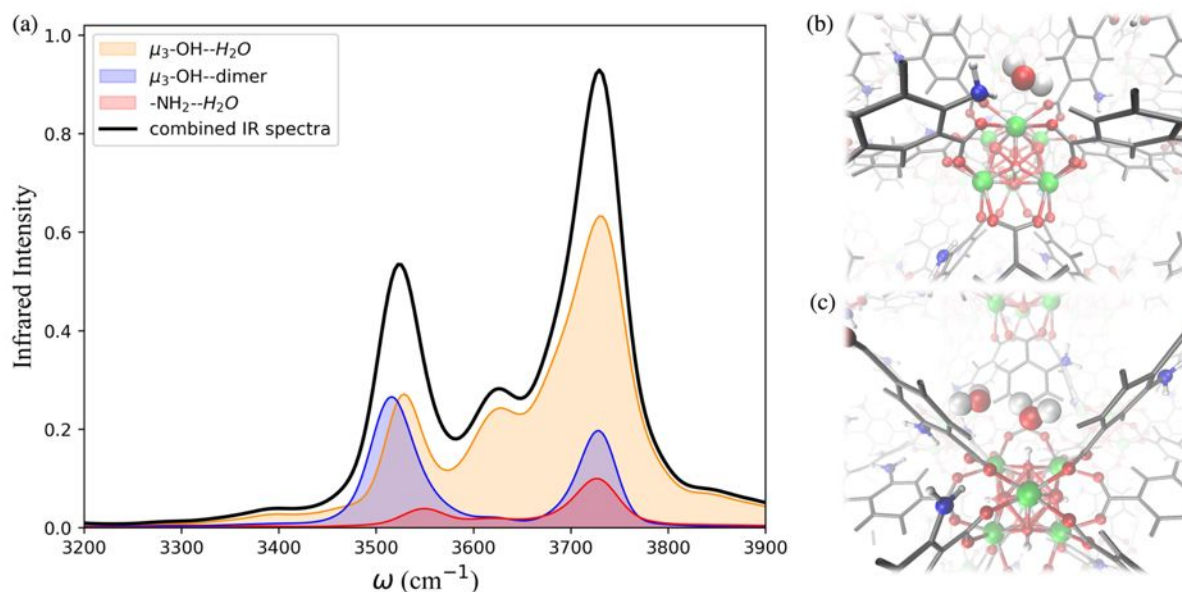


Figure 7: (a) Breakdown of the contributions to the IR spectrum of UiO-66-NH₂ at 10% relative humidity (RH) from single water molecules locating around the $\mu_3\text{-OH}$ site, water interacting with the -NH_2 functional group, and water dimers occupying the $\mu_3\text{-OH}$ sites, and the combined IR spectra resulting from summing these contributions; MD simulation snapshots showing (b) the water locating around the -NH_2 functional group and O_{linker} ; (c) the water dimer locating around the $\mu_3\text{-OH}$ interaction sites. Zr atoms are represented by green spheres, N atoms by blue spheres, O atoms by red spheres, H atoms by white spheres, and the benzene rings by grey lines.

The IR spectra calculated for the functionalized MOFs (Figure 5) show similar profiles to the IR spectra of UiO-66 with some variations caused by the dipole moment induced by the presence of functional groups within the MOFs. In order to understand which interactions are responsible for the different features of the IR spectra for the functionalized MOFs we analyzed the contributions from water interacting with the different sites of the UiO-66 variants at 10% RH (Figure 6a and 7a). In these MOFs, $\sim 10\%$ of water is located around the O_{linker} sites. Since the -NH_2 and -OH functional groups are located close to the O_{linker} , the water molecules at these sites can simultaneously interact with the adjacent -OH and -NH_2 functional groups. Thus, in addition to the non-hydrogen-bonded ($\sim 3713 \text{ cm}^{-1}$) and hydrogen-bonded O-H stretch ($\sim 3582 \text{ cm}^{-1}$) associated with a hydrogen-bond donor, the O-H stretch vibrations of the water molecules located near the O_{linker} in UiO-66 (Figure 4b), also report on the vibrations of the -

OH and -NH₂ functional groups due to electric couplings (spectral features at ~3550 cm⁻¹ in Figure 6a and 7a). In UiO-66-OH, the remaining water molecules are bonded to the μ₃-OH sites (~57%), or form dimers near the μ₃-OH sites (33%). Similar results were obtained for UiO-66-NH₂, with 63% of the water molecules involved in μ₃-OH···H₂O interactions and 27% in water dimers hydrogen-bonded to the μ₃-OH sites. Overall, while the μ₃-OH···H₂O interaction remains the preferred interaction, there are more water dimers formed in the functionalized MOFs compared to UiO-66. The spectral feature corresponding to the hydrogen-bonded O-H stretch in the water dimers occurs at a lower frequency in UiO-66-OH (3492 cm⁻¹) relative to UiO-66-NH₂ (3515 cm⁻¹) as shown in Figure 5 at both 10% and 20% RH. This is due to water interacting with the -OH functional groups being more polarized and forming stronger hydrogen-bonds with the water hydrogen-bonded to the μ₃-OH sites. This finding aligns with the calculated RDFs showing that -NH₂ interacts less strongly with water relative to -OH. Overall, the formation of more water dimers and larger polarization effects associated with the -OH group are responsible for the broadening of the hydrogen-bonded O-H stretching signal observed in -OH functionalized MOFs compared to UiO-66.

Another change in the IR spectra of the functionalized MOFs is that the signal corresponding to non-hydrogen-bonded O-H stretching vibrations of water is slightly redshifted to 3709 cm⁻¹ (Figure 5a) compared to UiO-66 (3723 cm⁻¹). This redshift can be explained by the fact that water bonded to the μ₃-OH sites in the functionalized MOFs has a higher tendency to donate hydrogen bonds to either water (thus forming dimers) or nearby functional groups. This leads to a greater contribution of non-hydrogen-bonded O-H stretching from hydrogen-bond-donating molecules in the spectra of the functionalized MOFs relative to UiO-66 (mostly asymmetric O-H stretch contribution from hydrogen-bond accepting waters above 3700 cm⁻¹, Figure 4b). This explanation is supported by the fact that the peak corresponding to the non-hydrogen-bonded O-H stretch of μ₃-OH···H₂O in the IR spectra of

water in the functionalized MOFs (yellow curve in Figure 6a and 7a) arises at a slightly lower frequency (3713 cm^{-1}) than the same peak (3743 cm^{-1}) in the UiO-66 spectrum (yellow curve in Figure 4b). This observation is consistent with the study performed by Zhang et al. that reported the non-hydrogen-bonded signal of a hydrogen-bond donating water molecule at a lower frequency than the asymmetric stretch of a hydrogen-bond accepting water molecule.⁸⁴ Thus, we find that the presence of the -OH and -NH₂ functional groups can (1) provide an additional attractive force for water to locate near the O_{linker} atoms and (2) stabilize the formation of water dimers. The former aids the formation of water clusters within the octahedral pores, while the latter allows water to form hydrogen-bonded chains anchored in the tetrahedral pores (where the strongest μ_3 -OH adsorption sites are located) and reaching into the octahedral pores. Both features seed the formation of water clusters within the larger octahedral pores, thus explaining why the burst uptake of water is observed at lower RH for the functionalized MOFs in several experimental studies.^{20,85,86}

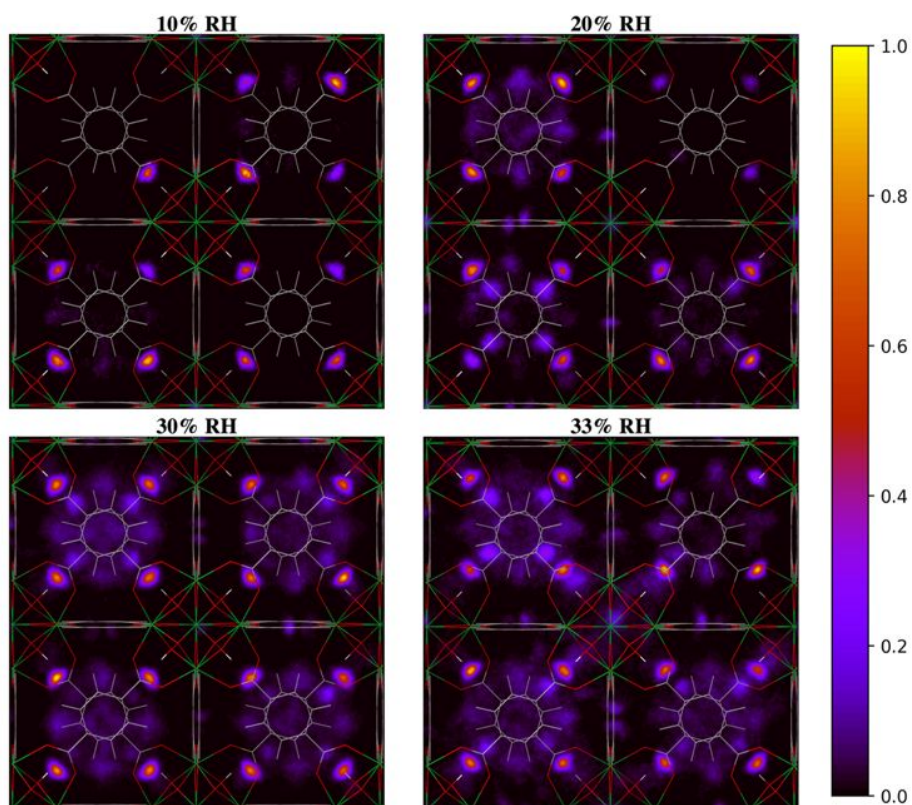


Figure 8: Two-dimensional density distribution maps for water within UiO-66 at 10-40% relative humidity (RH) along the *xy*-plane. Refer to Figure 1b to identify the position of the different pores and relevant interaction sites in the density maps. The scale bar indicates the density of water relative to the highest density region in the unit cell.

The two-dimensional density distribution maps of water within UiO-66 when RH = 10-40% provide further insights into the pore filling process. At low water loading (RH = 10%, Figure 8), the water is predominantly located at the μ_3 -OH sites in the tetrahedral pores. This aligns with our RDF results and predicted IR spectra, as well as previous findings in the literature, showing that at low water loading water occupies the tetrahedral pores first.^{13,28} Subsequent adsorbed water (RH = 20-30%) tends to form hydrogen-bonded networks with water molecules adsorbed at the μ_3 -OH sites within the tetrahedral pores. This results in water being preferentially located in the tetrahedral pores at these RH levels. Moreover, the water molecules tend to fill the tetrahedral pores that already contain water molecules rather than evenly distribute across all tetrahedral pores (Figure S8), suggesting that the formation of water

clusters stabilizes the water molecules within the tetrahedral pores. This observation is consistent with the IR spectra showing that the extended formation of hydrogen-bonded water chains is mainly responsible for the IR signal at 20% RH (Figure 4). Due to the symmetry of the UiO-66 framework, water clusters can form in any of the tetrahedral pores without a bias for specific ones (Figure S8). A similar phenomenon also occurs at 30% RH, where the formation of water clusters is preferred within the tetrahedral pores. However, the tetrahedral pores become unable to accommodate the water molecules as water loading increases beyond 30% RH (Figure 8). The additional water molecules tend to diffuse across the octahedral cavities interconnecting the tetrahedral pores and achieve a relatively more even distribution compared to water within UiO-66 at 20% RH. As the RH increases beyond 30%, water clusters start to form within the octahedral pores as shown in Figure 8. This RH level corresponds to the adsorption step (burst uptake of water) in the experimental adsorption isotherm (Figure 1a).¹¹ Thus, we conclude that the hydrogen-bonded chains of water anchoring on the μ_3 -OH sites in the tetrahedral pores and reaching into the octahedral pores provide the driving force for water clusters to form in the larger octahedral cavities, resulting in the burst uptake of water.

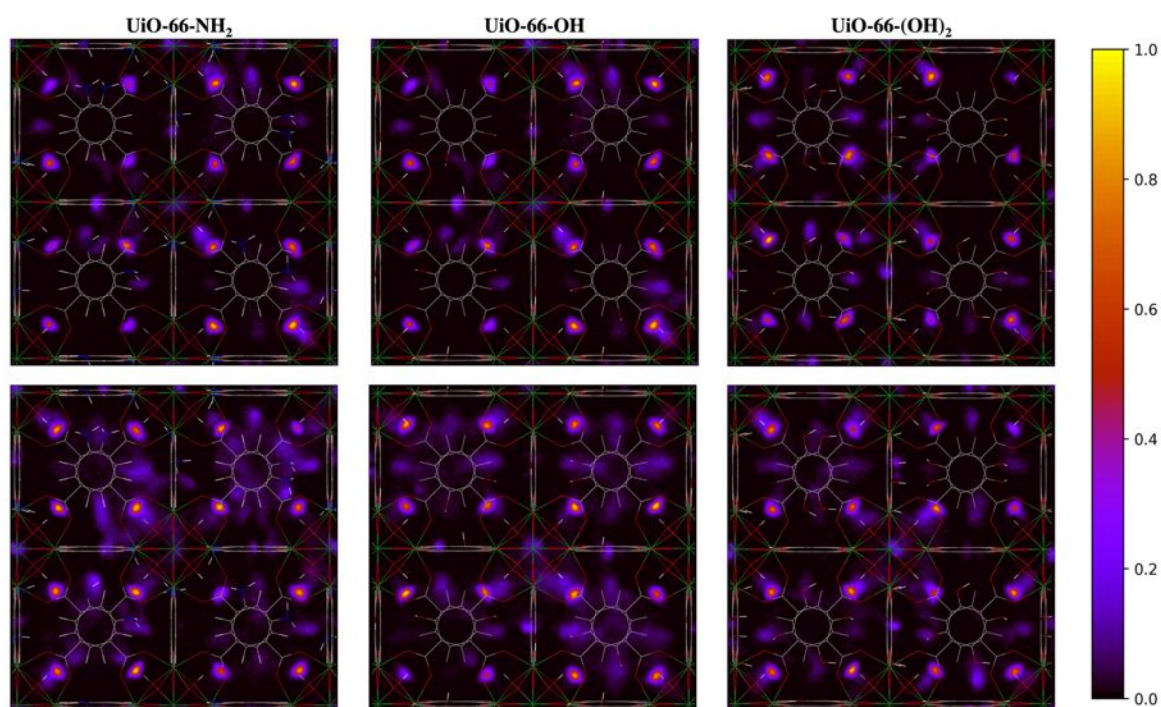


Figure 9: Two-dimensional density distribution maps for water within UiO-66-NH₂, UiO-66-OH, UiO-66-(OH)₂ with the same number of water molecules per unit cell as UiO-66 at 20% (top panel) and 30% (bottom panel) relative humidity (RH) along the xy-plane. Refer to Figure 1b to identify the position of the different pores and relevant interaction sites in the density maps. The scale bar indicates the density of water relative to the highest density region in the unit cell.

The two-dimensional density distribution maps for the functionalized MOFs show that, although water preferentially occupies the μ_3 -OH sites at low water loading, some water molecules are located near the functional groups of the linkers at 20% RH (Figure 9). Moreover, water molecules are distributed more evenly across the framework compared to UiO-66 at the same water loading. In fact, significant numbers of water molecules are in the octahedral pores in the presence of functional groups (Figure 9) compared to unfunctionalized UiO-66 at 30% RH (Figure 8). This result aligns with the IR spectra, which indicate that the presence of functional groups favors the formation of H₂O \cdots H₂O hydrogen-bonded chains that facilitate the diffusion of water molecules across the pores and help stabilize water near the O_{linker} interaction sites within the octahedral pores. Overall, these results provide a molecular-level

understanding of why functionalized UiO-66 MOFs show an abrupt increase in water uptake at lower water loadings relative to UiO-66.

Conclusions

The UiO-66 MOF is a promising material for atmospheric water harvesting and experimental studies have demonstrated that its adsorption performance at low RH (10-30%) can be further improved *via* the introduction of hydrophilic functional groups.^{7,20,86} Molecular-level insights into the interaction between water and MOFs are required to maximise the performance of these materials in water harvesting and use this technology at the industrial scale. In this work, we developed MD force field models for UiO-66 and its -NH₂, -OH and -(OH)₂ functionalized derivatives based on results from DFT calculations and experimental IR spectra. We then used MD simulations to compute the RDFs, IR spectra, and two-dimensional density distribution maps of water in the MOFs to gain a molecular-level understanding of water adsorption in UiO-66 and the influence of functionalization on this process. The pore filling process initiates at the μ_3 -OH sites, which have the highest affinity for water in UiO-66 and its functionalized derivatives. When an adequate amount of water has been adsorbed and the tetrahedral pores have been filled as RH increases, hydrogen-bonded water chains anchoring on the μ_3 -OH sites in the tetrahedral pores and reaching into the octahedral pores start to form. This phenomenon can be linked to the burst uptake of water shown in the experimental adsorption isotherm in UiO-66.¹¹ The presence of hydrophilic functional groups such as -OH provides an additional driving force for the formation of hydrogen-bonded water chains leading to the octahedral pores being filled with water at lower relative humidity. In addition to functional groups, recent studies have demonstrated that missing linker and missing cluster defects that are commonly present in UiO-66 can significantly increase its adsorptive

performance.^{12,13,87} Work is currently underway in our group to develop an accurate force field for defective UiO-66 and study its interaction with water. Overall, the present work provides a molecular-level understanding of why the functionalized MOFs show the adsorption step to occur at lower RH compared to unfunctionalized UiO-66. This knowledge can be used for the design of improved MOFs for water harvesting.

Supporting Information Available

Additional computational details for the DFT and MD calculations as well as force field development and benchmarking; additional RDF plots and two-dimensional density distribution maps for water within UiO-66 and its functionalized derivatives.

Conflicts of interest

There are no conflicts of interest to declare.

Acknowledgements

The research by J.Z. is supported by an Australian Government Research Training Program (RTP) Scholarship. F.P. was supported by the Department of Energy, Basic Energy Science (BES) Office through award no. DE-SC0019333. We are grateful for computational resources and services from the National Computational Infrastructure (NCI), provided by the Australian Government under the National Computational Merit Allocation Scheme, and the computational cluster Katana supported by Research Technology Services at UNSW Sydney. Ching-Hwa Ho, Kelly M. Hunter, and Hilliary O. Frank are acknowledged for helpful suggestions and training during this project.

References

- (1) Mekonnen, M. M.; Hoekstra, A. Y. Four Billion People Facing Severe Water Scarcity. *Sci Adv* **2016**, *2* (2). <https://doi.org/10.1126/sciadv.1500323>.
- (2) Voulvoulis, N. Water Reuse from a Circular Economy Perspective and Potential Risks from an Unregulated Approach. *Curr Opin Environ Sci Health* **2018**, *2*, 32–45. <https://doi.org/10.1016/j.coesh.2018.01.005>.
- (3) P. Gleick, et al. (edited by S. H. S. Water Resources. In *Encyclopaedia of Climate and Weather*; Oxford University Press: New York, 1996; Vol. 2, pp 817–823.
- (4) Zhou, X.; Lu, H.; Zhao, F.; Yu, G. Atmospheric Water Harvesting: A Review of Material and Structural Designs. *ACS Mater Lett* **2020**, *2* (7), 671–684. <https://doi.org/10.1021/acsmaterialslett.0c00130>.
- (5) Klemm, O.; Schemenauer, R. S.; Lummerich, A.; Cereceda, P.; Marzol, V.; Corell, D.; van Heerden, J.; Reinhard, D.; Gherezghiher, T.; Olivier, J.; Osses, P.; Sarsour, J.; Frost, E.; Estrela, M. J.; Valiente, J. A.; Fessehaye, G. M. Fog as a Fresh-Water Resource: Overview and Perspectives. *Ambio* **2012**, *41* (3), 221–234. <https://doi.org/10.1007/s13280-012-0247-8>.
- (6) Jin, Y.; Zhang, L.; Wang, P. Atmospheric Water Harvesting: Role of Surface Wettability and Edge Effect. *Global Challenges* **2017**, *1* (4), 1700019. <https://doi.org/10.1002/gch2.201700019>.
- (7) Hanikel, N.; Prévot, M. S.; Yaghi, O. M. MOF Water Harvesters. *Nat Nanotechnol* **2020**, *15* (5), 348–355. <https://doi.org/10.1038/s41565-020-0673-x>.
- (8) Stock, N.; Biswas, S. Synthesis of Metal-Organic Frameworks (MOFs): Routes to Various MOF Topologies, Morphologies, and Composites. *Chemical Reviews*. February 8, 2012, pp 933–969. <https://doi.org/10.1021/cr200304e>.
- (9) Jasuja, H.; Walton, K. S. Effect of Catenation and Basicity of Pillared Ligands on the Water Stability of MOFs. *Dalton Transactions* **2013**, *42* (43), 15421. <https://doi.org/10.1039/c3dt51819a>.
- (10) Cavka, J. H.; Jakobsen, S.; Olsbye, U.; Guillou, N.; Lamberti, C.; Bordiga, S.; Lillerud, K. P. A New Zirconium Inorganic Building Brick Forming Metal Organic Frameworks with Exceptional Stability. *J Am Chem Soc* **2008**, *130* (42), 13850–13851. <https://doi.org/10.1021/ja8057953>.
- (11) Furukawa, H.; Gándara, F.; Zhang, Y. B.; Jiang, J.; Queen, W. L.; Hudson, M. R.; Yaghi, O. M. Water Adsorption in Porous Metal-Organic Frameworks and Related Materials. *J Am Chem Soc* **2014**, *136* (11), 4369–4381. <https://doi.org/10.1021/ja500330a>.
- (12) Feng, Y.; Chen, Q.; Jiang, M.; Yao, J. Tailoring the Properties of UiO-66 through Defect Engineering: A Review. *Industrial and Engineering Chemistry Research*. American Chemical Society September 25, 2019, pp 17646–17659. <https://doi.org/10.1021/acs.iecr.9b03188>.
- (13) Ghosh, P.; Colón, Y. J.; Snurr, R. Q. Water Adsorption in UiO-66: The Importance of Defects. *Chem. Commun.* **2014**, *50* (77), 11329–11331. <https://doi.org/10.1039/C4CC04945D>.
- (14) Shan, B.; McIntyre, S. M.; Armstrong, M. R.; Shen, Y.; Mu, B. Investigation of Missing-Cluster Defects in UiO-66 and Ferrocene Deposition into Defect-Induced Cavities. *Ind Eng Chem Res* **2018**, *57* (42). <https://doi.org/10.1021/acs.iecr.8b03516>.
- (15) Hyunho, K.; Sungwoo, Y.; R, R. S.; Shankar, N.; A, K. E.; Hiroyasu, F.; S, U. A.; M, Y. O.; N, W. E. Water Harvesting from Air with Metal-Organic Frameworks Powered by Natural Sunlight. *Science (1979)* **2017**, *356* (6336), 430–434. <https://doi.org/10.1126/science.aam8743>.

- (16) Kim, H.; Yang, S.; Rao, S. R.; Narayanan, S.; Kapustin, E. A.; Furukawa, H.; Umans, A. S.; Yaghi, O. M.; Wang, E. N. *RENEWABLE RESOURCES Water Harvesting from Air with Metal-Organic Frameworks Powered by Natural Sunlight*, 2017; Vol. 356.
- (17) Fathieh, F.; Kalmutzki, M. J.; Kapustin, E. A.; Waller, P. J.; Yang, J.; Yaghi, O. M. Practical Water Production from Desert Air. *Sci Adv* **2018**, *4* (6). <https://doi.org/10.1126/sciadv.aat3198>.
- (18) Jeremias, F.; Lozan, V.; Henninger, S. K.; Janiak, C. Programming MOFs for Water Sorption: Amino-Functionalized MIL-125 and UiO-66 for Heat Transformation and Heat Storage Applications. *Dalton Transactions* **2013**, *42* (45), 15967. <https://doi.org/10.1039/c3dt51471d>.
- (19) Canivet, J.; Bonnefoy, J.; Daniel, C.; Legrand, A.; Coasne, B.; Farrusseng, D. Structure–Property Relationships of Water Adsorption in Metal–Organic Frameworks. *New J. Chem.* **2014**, *38* (7), 3102–3111. <https://doi.org/10.1039/C4NJ00076E>.
- (20) Tang, X.; Luo, Y.; Zhang, Z.; Ding, W.; Liu, D.; Wang, J.; Guo, L.; Wen, M. Effects of Functional Groups of –NH₂ and –NO₂ on Water Adsorption Ability of Zr-Based MOFs (UiO-66). *Chem Phys* **2021**, *543*. <https://doi.org/10.1016/j.chemphys.2021.111093>.
- (21) Lu, F.-F.; Gu, X.-W.; Wu, E.; Li, B.; Qian, G. Systematic Evaluation of Water Adsorption in Isorecticular UiO-Type Metal–Organic Frameworks. *J Mater Chem A Mater* **2023**, *11* (3), 1246–1255. <https://doi.org/10.1039/D2TA07392G>.
- (22) Winarta, J.; Shan, B.; Mcintyre, S. M.; Ye, L.; Wang, C.; Liu, J.; Mu, B. A Decade of UiO-66 Research: A Historic Review of Dynamic Structure, Synthesis Mechanisms, and Characterization Techniques of an Archetypal Metal–Organic Framework. *Cryst Growth Des* **2020**, *20* (2). <https://doi.org/10.1021/acs.cgd.9b00955>.
- (23) Wiersum, A. D.; Soubeyrand-Lenoir, E.; Yang, Q.; Moulin, B.; Guillerm, V.; Yahia, M. ben; Bourrelly, S.; Vimont, A.; Miller, S.; Vagner, C.; Daturi, M.; Clet, G.; Serre, C.; Maurin, G.; Llewellyn, P. L. An Evaluation of UiO-66 for Gas-Based Applications. *Chem Asian J* **2011**, *6* (12), 3270–3280. <https://doi.org/10.1002/asia.201100201>.
- (24) Mancuso, J. L.; Mroz, A. M.; Le, K. N.; Hendon, C. H. Electronic Structure Modeling of Metal–Organic Frameworks. *Chem Rev* **2020**, *120* (16), 8641–8715. <https://doi.org/10.1021/acs.chemrev.0c00148>.
- (25) Evans, J. D.; Fraux, G.; Gaillac, R.; Kohen, D.; Trouselet, F.; Vanson, J.-M.; Coudert, F.-X. Computational Chemistry Methods for Nanoporous Materials. *Chemistry of Materials* **2017**, *29* (1), 199–212. <https://doi.org/10.1021/acs.chemmater.6b02994>.
- (26) Coudert, F.-X.; Fuchs, A. H. Computational Characterization and Prediction of Metal–Organic Framework Properties. *Coord Chem Rev* **2016**, *307*, 211–236. <https://doi.org/10.1016/j.ccr.2015.08.001>.
- (27) Rappé, A. K.; Casewit, C. J.; Colwell, K. S.; Goddard, W. A.; Skiff, W. M. UFF, a Full Periodic Table Force Field for Molecular Mechanics and Molecular Dynamics Simulations. *J Am Chem Soc* **1992**, *114* (25), 10024–10035. <https://doi.org/10.1021/ja00051a040>.
- (28) Wang, S.; Zhou, G.; Sun, Y.; Huang, L. A Computational Study of Water in UiO-66 Zr-MOFs: Diffusion, Hydrogen Bonding Network, and Confinement Effect. *AIChE Journal* **2021**, *67* (3). <https://doi.org/10.1002/aic.17035>.
- (29) Caratelli, C.; Hajek, J.; Meijer, E. J.; Waroquier, M.; Van Speybroeck, V. Dynamic Interplay between Defective UiO-66 and Protic Solvents in Activated Processes. *Chemistry - A European Journal* **2019**, *25* (67), 15315–15325. <https://doi.org/10.1002/chem.201903178>.

- (30) Shukla, P. B.; Johnson, J. K. Impact of Loading-Dependent Intrinsic Framework Flexibility on Adsorption in UiO-66. *The Journal of Physical Chemistry C* **2022**, *126* (41), 17699–17711. <https://doi.org/10.1021/acs.jpcc.2c04629>.
- (31) Babin, V.; Leforestier, C.; Paesani, F. Development of a “First Principles” Water Potential with Flexible Monomers: Dimer Potential Energy Surface, VRT Spectrum, and Second Virial Coefficient. *J Chem Theory Comput* **2013**, *9* (12). <https://doi.org/10.1021/ct400863t>.
- (32) Babin, V.; Medders, G. R.; Paesani, F. Development of a “First Principles” Water Potential with Flexible Monomers. II: Trimer Potential Energy Surface, Third Virial Coefficient, and Small Clusters. *J Chem Theory Comput* **2014**, *10* (4). <https://doi.org/10.1021/ct500079y>.
- (33) Medders, G. R.; Babin, V.; Paesani, F. Development of a “First-Principles” Water Potential with Flexible Monomers. III. Liquid Phase Properties. *J Chem Theory Comput* **2014**, *10* (8). <https://doi.org/10.1021/ct5004115>.
- (34) Paesani, F. Getting the Right Answers for the Right Reasons: Toward Predictive Molecular Simulations of Water with Many-Body Potential Energy Functions. *Acc Chem Res* **2016**, *49* (9), 1844–1851. <https://doi.org/10.1021/acs.accounts.6b00285>.
- (35) Reddy, S. K.; Straight, S. C.; Bajaj, P.; Huy Pham, C.; Riera, M.; Moberg, D. R.; Morales, M. A.; Knight, C.; Götz, A. W.; Paesani, F. On the Accuracy of the MB-Pol Many-Body Potential for Water: Interaction Energies, Vibrational Frequencies, and Classical Thermodynamic and Dynamical Properties from Clusters to Liquid Water and Ice. *J Chem Phys* **2016**, *145* (19). <https://doi.org/10.1063/1.4967719>.
- (36) Medders, G. R.; Paesani, F. Dissecting the Molecular Structure of the Air/Water Interface from Quantum Simulations of the Sum-Frequency Generation Spectrum. *J Am Chem Soc* **2016**, *138* (11), 3912–3919. <https://doi.org/10.1021/jacs.6b00893>.
- (37) Medders, G. R.; Paesani, F. Infrared and Raman Spectroscopy of Liquid Water through “First-Principles” Many-Body Molecular Dynamics. *J Chem Theory Comput* **2015**, *11* (3), 1145–1154. <https://doi.org/10.1021/ct501131j>.
- (38) Goldberg, D. E. *Genetic Algorithms in Search, Optimization and Machine Learning*, 1st ed.; Addison-Wesley Longman Publishing Co., Inc.: USA, 1989.
- (39) Kohn, W.; Sham, L. J. Self-Consistent Equations Including Exchange and Correlation Effects. *Physical Review* **1965**, *140* (4A), A1133–A1138. <https://doi.org/10.1103/PhysRev.140.A1133>.
- (40) Hohenberg, P.; Kohn, W. Inhomogeneous Electron Gas. *Physical Review* **1964**, *136* (3B), B864–B871. <https://doi.org/10.1103/PhysRev.136.B864>.
- (41) Kresse, G.; Hafner, J. Ab Initio Molecular Dynamics for Liquid Metals. *Phys Rev B* **1993**, *47* (1), 558–561. <https://doi.org/10.1103/PhysRevB.47.558>.
- (42) Kresse, G.; Hafner, J. Ab Initio Molecular-Dynamics Simulation of the Liquid-Metal--Amorphous-Semiconductor Transition in Germanium. *Phys Rev B* **1994**, *49* (20), 14251–14269. <https://doi.org/10.1103/PhysRevB.49.14251>.
- (43) Kresse, G.; Furthmüller, J. Efficient Iterative Schemes for *Ab Initio* Total-Energy Calculations Using a Plane-Wave Basis Set. *Phys Rev B* **1996**, *54* (16), 11169–11186. <https://doi.org/10.1103/PhysRevB.54.11169>.
- (44) Kresse, G.; Furthmüller, J. Efficiency of Ab-Initio Total Energy Calculations for Metals and Semiconductors Using a Plane-Wave Basis Set. *Comput Mater Sci* **1996**, *6* (1), 15–50. [https://doi.org/10.1016/0927-0256\(96\)00008-0](https://doi.org/10.1016/0927-0256(96)00008-0).
- (45) Johnson, E. R.; Becke, A. D. A Post-Hartree-Fock Model of Intermolecular Interactions: Inclusion of Higher-Order Corrections. *J Chem Phys* **2006**, *124* (17), 174104. <https://doi.org/10.1063/1.2190220>.

- (46) Grimme, S.; Ehrlich, S.; Goerigk, L. Effect of the Damping Function in Dispersion Corrected Density Functional Theory. *J Comput Chem* **2011**, *32* (7), 1456–1465. <https://doi.org/10.1002/jcc.21759>.
- (47) Grimme, S.; Antony, J.; Ehrlich, S.; Krieg, H. A Consistent and Accurate *Ab Initio* Parametrization of Density Functional Dispersion Correction (DFT-D) for the 94 Elements H-Pu. *J Chem Phys* **2010**, *132* (15), 154104. <https://doi.org/10.1063/1.3382344>.
- (48) Mardirossian, N.; Head-Gordon, M. ω B97X-V: A 10-Parameter, Range-Separated Hybrid, Generalized Gradient Approximation Density Functional with Nonlocal Correlation, Designed by a Survival-of-the-Fittest Strategy. *Physical Chemistry Chemical Physics* **2014**, *16* (21), 9904. <https://doi.org/10.1039/c3cp54374a>.
- (49) Najibi, A.; Goerigk, L. The Nonlocal Kernel in van Der Waals Density Functionals as an Additive Correction: An Extensive Analysis with Special Emphasis on the B97M-V and ω B97M-V Approaches. *J Chem Theory Comput* **2018**, *14* (11), 5725–5738. <https://doi.org/10.1021/acs.jctc.8b00842>.
- (50) Neese, F. The ORCA Program System. *WIREs Computational Molecular Science* **2012**, *2* (1), 73–78. <https://doi.org/10.1002/wcms.81>.
- (51) Neese, F. Prediction of Molecular Properties and Molecular Spectroscopy with Density Functional Theory: From Fundamental Theory to Exchange-Coupling. *Coord Chem Rev* **2009**, *253* (5–6), 526–563. <https://doi.org/10.1016/j.ccr.2008.05.014>.
- (52) Neese, F. Software Update: The <sc>ORCA</Sc> Program System—Version 5.0. *WIREs Computational Molecular Science* **2022**. <https://doi.org/10.1002/wcms.1606>.
- (53) Weigend, F.; Ahlrichs, R. Balanced Basis Sets of Split Valence, Triple Zeta Valence and Quadruple Zeta Valence Quality for H to Rn: Design and Assessment of Accuracy. *Physical Chemistry Chemical Physics* **2005**, *7* (18), 3297. <https://doi.org/10.1039/b508541a>.
- (54) Weigend, F. Accurate Coulomb-Fitting Basis Sets for H to Rn. *Physical Chemistry Chemical Physics* **2006**, *8* (9), 1057. <https://doi.org/10.1039/b515623h>.
- (55) Andrae, D.; Hühnermann, U.; Dolg, M.; Stoll, H.; Preußner, H. Energy-Adjusted *Ab Initio* Pseudopotentials for the Second and Third Row Transition Elements. *Theor Chim Acta* **1990**, *77* (2), 123–141. <https://doi.org/10.1007/BF01114537>.
- (56) Wang, J.; Wolf, R. M.; Caldwell, J. W.; Kollman, P. A.; Case, D. A. Development and Testing of a General Amber Force Field. *J Comput Chem* **2004**, *25* (9), 1157–1174. <https://doi.org/10.1002/jcc.20035>.
- (57) Fang, Y.; Zhang, L.; Zhao, Q.; Wang, X.; Jia, X. Highly Selective Visible-Light Photocatalytic Benzene Hydroxylation to Phenol Using a New Heterogeneous Photocatalyst UiO-66-NH₂-SA-V. *Catal Letters* **2019**, *149* (9), 2408–2414. <https://doi.org/10.1007/s10562-019-02842-3>.
- (58) Veisi, H.; Abrifam, M.; Kamangar, S. A.; Pirhayati, M.; Saremi, S. G.; Noroozi, M.; Tamoradi, T.; Karmakar, B. Pd Immobilization Biguanidine Modified Zr-UiO-66 MOF as a Reusable Heterogeneous Catalyst in Suzuki–Miyaura Coupling. *Sci Rep* **2021**, *11* (1), 21883. <https://doi.org/10.1038/s41598-021-00991-3>.
- (59) Hadjiivanov, K. I.; Panayotov, D. A.; Mihaylov, M. Y.; Ivanova, E. Z.; Chakarova, K. K.; Andonova, S. M.; Drenchev, N. L. Power of Infrared and Raman Spectroscopies to Characterize Metal-Organic Frameworks and Investigate Their Interaction with Guest Molecules. *Chemical Reviews*. American Chemical Society February 10, 2021, pp 1286–1424. <https://doi.org/10.1021/acs.chemrev.0c00487>.
- (60) Rada, Z. H.; Abid, H. R.; Shang, J.; Sun, H.; He, Y.; Webley, P.; Liu, S.; Wang, S. Functionalized UiO-66 by Single and Binary (OH)₂ and NO₂ Groups for Uptake of

- CO₂ and CH₄. *Ind Eng Chem Res* **2016**, *55* (29), 7924–7932. <https://doi.org/10.1021/acs.iecr.5b04061>.
- (61) Moghaddam, Z. S.; Kaykhahi, M.; Khajeh, M.; Oveisi, A. R. Synthesis of UiO-66-OH Zirconium Metal-Organic Framework and Its Application for Selective Extraction and Trace Determination of Thorium in Water Samples by Spectrophotometry. *Spectrochim Acta A Mol Biomol Spectrosc* **2018**, *194*, 76–82. <https://doi.org/10.1016/j.saa.2018.01.010>.
- (62) Rieth, A. J.; Hunter, K. M.; Dincă, M.; Paesani, F. Hydrogen Bonding Structure of Confined Water Templated by a Metal-Organic Framework with Open Metal Sites. *Nat Commun* **2019**, *10* (1). <https://doi.org/10.1038/s41467-019-12751-z>.
- (63) Kumar, A.; Kumar, P. Gas Phase Acidity of Water Clusters. *Physical Chemistry Chemical Physics* **2022**, *24* (30), 18236–18244. <https://doi.org/10.1039/D2CP01578A>.
- (64) Yagasaki, T.; Iwahashi, K.; Saito, S.; Ohmine, I. A Theoretical Study on Anomalous Temperature Dependence of PK_w of Water. *J Chem Phys* **2005**, *122* (14), 144504. <https://doi.org/10.1063/1.1878712>.
- (65) *NIST web page*. <https://webbook.nist.gov/> (accessed 2023-06-21).
- (66) Kim, K. C.; Yu, D.; Snurr, R. Q. Computational Screening of Functional Groups for Ammonia Capture in Metal–Organic Frameworks. *Langmuir* **2013**, *29* (5), 1446–1456. <https://doi.org/10.1021/la3045237>.
- (67) Jiang, J.; Yaghi, O. M. Brønsted Acidity in Metal–Organic Frameworks. *Chem Rev* **2015**, *115* (14), 6966–6997. <https://doi.org/10.1021/acs.chemrev.5b00221>.
- (68) Ibrahim, A. H.; El-Mehalmey, W. A.; Haikal, R. R.; Safy, M. E. A.; Amin, M.; Shatla, H. R.; Karakalos, S. G.; Alkordi, M. H. Tuning the Chemical Environment within the UiO-66-NH₂ Nanocages for Charge-Dependent Contaminant Uptake and Selectivity. *Inorg Chem* **2019**, *58* (22), 15078–15087. <https://doi.org/10.1021/acs.inorgchem.9b01611>.
- (69) Wagner, J. C.; Hunter, K. M.; Paesani, F.; Xiong, W. Water Capture Mechanisms at Zeolitic Imidazolate Framework Interfaces. *J Am Chem Soc* **2021**, *143* (50), 21189–21194. <https://doi.org/10.1021/jacs.1c09097>.
- (70) Hunter, K. M.; Wagner, J. C.; Kalaj, M.; Cohen, S. M.; Xiong, W.; Paesani, F. Simulation Meets Experiment: Unraveling the Properties of Water in Metal-Organic Frameworks through Vibrational Spectroscopy. *Journal of Physical Chemistry C* **2021**, *125* (22), 12451–12460. <https://doi.org/10.1021/acs.jpcc.1c03145>.
- (71) Lorentz, H. A. Ueber Die Anwendung Des Satzes Vom Virial in Der Kinetischen Theorie Der Gase. *Ann Phys* **1881**, *248* (1), 127–136. <https://doi.org/10.1002/andp.18812480110>.
- (72) Abascal, J. L. F.; Vega, C. A General Purpose Model for the Condensed Phases of Water: TIP4P/2005. *J Chem Phys* **2005**, *123* (23), 234505. <https://doi.org/10.1063/1.2121687>.
- (73) Ho, C.-H.; Valentine, M. L.; Chen, Z.; Xie, H.; Farha, O.; Xiong, W.; Paesani, F. Structure and Thermodynamics of Water Adsorption in NU-1500-Cr. *Commun Chem* **2023**, *6* (1), 70. <https://doi.org/10.1038/s42004-023-00870-0>.
- (74) Simon, S.; Duran, M.; Dannenberg, J. J. Effect of Basis Set Superposition Error on the Water Dimer Surface Calculated at Hartree-Fock, Møller-Plesset, and Density Functional Theory Levels. *Journal of Physical Chemistry A* **1999**, *103*, 1640–1643.
- (75) Simon, S.; Duran, M.; Dannenberg, J. J. How Does Basis Set Superposition Error Change the Potential Surfaces for Hydrogen-bonded Dimers? *J Chem Phys* **1996**, *105* (24), 11024–11031. <https://doi.org/10.1063/1.472902>.
- (76) Marenich, A. V.; Jerome, S. V.; Cramer, C. J.; Truhlar, D. G. Charge Model 5: An Extension of Hirshfeld Population Analysis for the Accurate Description of Molecular

- Interactions in Gaseous and Condensed Phases. *J Chem Theory Comput* **2012**, *8* (2), 527–541. <https://doi.org/10.1021/ct200866d>.
- (77) Frisch, M. J.; Trucks, G. W.; Schlegel, H. B.; Scuseria, G. E.; Robb, M. A.; Cheeseman, J. R.; Scalmani, G.; Barone, V.; Petersson, G. A.; Nakatsuji, H. Gaussian 16, 2016. *Gaussian Inc. Wallingford CT* **2016**.
- (78) Smith, W.; Forester, T. R. *DL_POLY_2.0: A General-Purpose Parallel Molecular Dynamics Simulation Package*; 1996.
- (79) Tuckerman, M. *Statistical Mechanics: Theory and Molecular Simulation*; Oxford university press, 2010.
- (80) Andrew, R. L. *Molecular Modeling Principles and Applications*. Prentice Hall, London **2001**.
- (81) Martínez, L.; Andrade, R.; Birgin, E. G.; Martínez, J. M. PACKMOL: A Package for Building Initial Configurations for Molecular Dynamics Simulations. *J Comput Chem* **2009**, *30* (13), 2157–2164. <https://doi.org/10.1002/jcc.21224>.
- (82) Bertie, J. E.; Lan, Z. Infrared Intensities of Liquids XX: The Intensity of the OH Stretching Band of Liquid Water Revisited, and the Best Current Values of the Optical Constants of H₂O(l) at 25°C between 15,000 and 1 Cm⁻¹. *Appl Spectrosc* **1996**, *50* (8), 1047–1057. <https://doi.org/10.1366/0003702963905385>.
- (83) Ramasesha, K.; de Marco, L.; Mandal, A.; Tokmakoff, A. Water Vibrations Have Strongly Mixed Intra- and Intermolecular Character. *Nat Chem* **2013**, *5* (11), 935–940. <https://doi.org/10.1038/nchem.1757>.
- (84) Zhang, B.; Yu, Y.; Zhang, Z.; Zhang, Y. Y.; Jiang, S.; Li, Q.; Yang, S.; Hu, H. S.; Zhang, W.; Dai, D.; Wu, G.; Li, J.; Zhang, D. H.; Yang, X.; Jiang, L. Infrared Spectroscopy of Neutral Water Dimer Based on a Tunable Vacuum Ultraviolet Free Electron Laser. *Journal of Physical Chemistry Letters* **2020**, *11* (3), 851–855. <https://doi.org/10.1021/acs.jpcllett.9b03683>.
- (85) Kim, S. I.; Yoon, T. U.; Kim, M. B.; Lee, S. J.; Hwang, Y. K.; Chang, J. S.; Kim, H. J.; Lee, H. N.; Lee, U. H.; Bae, Y. S. Metal-Organic Frameworks with High Working Capacities and Cyclic Hydrothermal Stabilities for Fresh Water Production. *Chemical Engineering Journal* **2016**, *286*, 467–475. <https://doi.org/10.1016/j.cej.2015.10.098>.
- (86) Schoenecker, P. M.; Carson, C. G.; Jasuja, H.; Flemming, C. J. J.; Walton, K. S. Effect of Water Adsorption on Retention of Structure and Surface Area of Metal-Organic Frameworks. *Ind Eng Chem Res* **2012**, *51* (18), 6513–6519. <https://doi.org/10.1021/ie202325p>.
- (87) Hernandez, A. F.; Impastato, R. K.; Hossain, M. I.; Rabideau, B. D.; Glover, T. G. Water Bridges Substitute for Defects in Amine-Functionalized UiO-66, Boosting CO₂ Adsorption. *Langmuir* **2021**, *37* (35), 10439–10449. <https://doi.org/10.1021/acs.langmuir.1c01149>.